# Chemical species tomographic imaging of the vapour fuel distribution in a compression-ignition engine

# Chemical species tomographic imaging of the vapour fuel distribution in a Compression Ignition engine

Stylianos-Alexios Tsekenis[1], Ramaswamy Kumara Gurubaran[3], Nigel Tait[2], Yannis Hardalupas[3], Alexander Taylor[3] and Hugh McCann[1]

[1]School of Engineering, The University of Edinburgh, UK
[2]Shell U.K. Limited, Shell Centre, London, UK
[3]Department of Mechanical Engineering, Imperial College London, UK

**Abstract**

This paper reports the first application of Chemical Species Tomography to visualise the in-cylinder fuel vapour concentration distribution during the mixing process in a compression ignition engine. The engine was operated in motored conditions using nitrogen aspiration, and fired conditions using a gasoline-like blend of 50% i-dodecane and 50% n-dodecane. The tomography system comprises 31 laser beams arranged in a co-planar grid located below the injector. A novel, robust data referencing scheme was employed to condition the acquired data for image reconstruction using the iterative Landweber algorithm. Tomographic images were acquired during the compression stroke at a rate of 13 frames per Crank Angle Degree within the same engine cycle at 1200 RPM. The temperature-dependent fuel evaporation rate and mixing evolution were observed at different injection timings and intake pressure and temperature conditions. An initial cross-validation of the tomographic images was performed with Planar Laser Induced Fluorescence images, showing good agreement in feature localisation and identification. This is the first time chemical species tomography using Near-IR spectroscopic absorption has been validated under engine conditions, and the first application of Chemical Species Tomography to a Compression Ignition engine.

**Corresponding author**

Stylianos-Alexios Tsekenis, School of Engineering, The University of Edinburgh, EH9 3FG, UK.
Email: a.tsekenis@ed.ac.uk

**Keywords**

Optical tomography, chemical species tomography, compression ignition, engine diagnostics, mixture preparation

## Introduction

The combustion process in Internal Combustion (IC) engines produces a multitude of reaction products, some of which are released into the atmosphere as gaseous and particulate emissions. Due to their detrimental effects, these are stringently regulated with increasingly challenging limits as published in the Euro 5/6 standards (EC 715/2007).

Compression Ignition (CI) engines provide high fuel efficiency at the expense of NOx and soot emissions. Formation of NOx occurs at low equivalence ratios ($\phi < 2$, where $\phi$ is the reciprocal of lambda) and high flame temperatures (> 2200 K). Conversely, soot (particulate matter, PM) is formed at high equivalence ratios and intermediate to high flame temperatures. The mixing and combustion process of fuel in a traditional CI engine passes through both of these regions thus leading to high levels of soot and NOx emissions. Furthermore, there is little control over the combustion process.

Various technologies have been developed to treat NOx and PM emissions. In particular, Diesel Particulate Filters (DPFs) remove PM from the exhaust, while Selective Catalytic Reduction (SCR) systems and Lean NOx traps reduce NOx emissions[1]. However, addition of after-treatment systems increases the overall complexity and cost of the diesel engine, offsetting the increased fuel efficiency. In addition, such technologies often impose impractical requirements on the owner of the vehicle such as driving at increased speed (diesel particulate filter regeneration) or refilling of a reactant tank (selective catalytic reduction)[2].

Advanced CI combustion schemes aim to carefully control the equivalence ratio and flame temperature and thus relax the requirements for after-treatment systems. Premixed Charge Compression Ignition (PCCI) and Homogeneous Charge Compression Ignition (HCCI) schemes promote mixing of the fuel-air charge prior to ignition. Compared to traditional CI operation, homogenised mixtures can produce less PM and NOx if the mixture is lean.

Current CI engine research[3,4] explores the application of fuels less prone to auto-ignition in order to control mixture homogeneity. Experiments using low cetane number fuels have been performed on a two-litre, single-cylinder engine indicating that a globally partially pre-mixed condition is desirable[4-6]. To enable this research, the ability to image the spatial distribution of fuel concentration is highly desirable.

Numerous diagnostic techniques exist for the in-cylinder visualisation and quantification of liquid and vapour fuel concentration distribution. These techniques have been reviewed extensively in literature[7,8], so we will restrict ourselves to only essential remarks here.

*Planar Laser-Induced Fluorescence*

Planar Laser Induced Fluorescence (PLIF) is a long-established and mature[9,12] and widely adopted for the measurement of the spatial distribution of hydrocarbon fuel in engines[10-12]. In brief, a PLIF setup consists of a laser source usually projecting pulsed light formed into a thin sheet which traverses the combustion chamber through an optical access ring. The laser wavelength (typically in the UV range) is chosen to match a spectroscopic transition of a tracer species previously mixed into the fuel; a fraction of the incident light is absorbed and re-emitted as fluorescence, the intensity of which is proportional to the concentration of the tracer species, typically selected to match the physical properties of the fuel. A high speed camera captures the fluorescence at 90° to the illumination plane, typically through an optical piston.

*Chemical Species Tomography by near-IR absorption*

It has been shown[13] that near-IR absorption is viable for Chemical Species Tomography (CST), exploiting the spectrally wide and relatively unstructured spectroscopic absorption feature that all partially or fully saturated hydrocarbons display near 1700 nm. In order to suppress non-species specific signals, a second beam is introduced as a reference and its wavelength chosen to experience attenuation only by non-resonant, non-chemically specific mechanisms. The reference beam is made to ideally traverse the same path as the measurement beam. The spectral separation of the measurement and reference wavelengths $\lambda_{meas}$ and $\lambda_{ref}$ respectively is minimised to suppress chromatic dispersion effects. Computation of the ratio of the two received intensities substantially suppresses the non-chemically specific effects. We refer to this two-wavelength scheme as Dual-Wavelength Ratiometric (DWR).

At a given wavelength $\lambda$, the received intensity is described by the general form of the Beer-Lambert law (equation 1).

$$I_r(\lambda) = I_o e^{-k(\lambda)\int_l c(x,y)\mathrm{dl}}.F + I_T \quad (1)$$

where $I_o$ is the initial intensity at launch, $k$ is the absorption coefficient [litres.mol$^{-1}$.cm$^{-1}$] and is assumed to be constant over the path length $l$ [cm] though the gas cloud of concentration $c(x, y)$. The exponent is termed the Path Concentration Integral (PCI). Attenuation that is not species specific is modelled by $F$ and the background thermal radiation noise is modelled by $I_T$.

The general form of the Beer-Lambert law (equation 1), solved for the PCI, can be expressed in terms of the received intensity at the measurement and reference wavelengths (equation 2).

$$\mathrm{PCI} = \int_L c(x,y)\mathrm{dL} = \frac{1}{k\lambda_{\mathrm{meas}} - k\lambda_{\mathrm{ref}}} \ln\left(\frac{I_{r(\lambda_{\mathrm{ref}})} - I_{T(\lambda_{\mathrm{ref}})}}{I_{r(\lambda_{\mathrm{meas}})} - I_{T(\lambda_{\mathrm{meas}})}} . \frac{I_{o(\lambda_{\mathrm{meas}})}}{I_{o(\lambda_{\mathrm{ref}})}}\right) \quad (2)$$

*Instrumentation system*

The instrumentation system has been described more fully in[14] and its spatial resolution performance previously quantified in[15]. It consists of two modulated laser sources at 1700 nm ($\lambda_{meas}$) and 1651 nm ($\lambda_{ref}$), combined using Wavelength-Division Multiplexing (WDM) and divided into 32 beams which are subsequently guided to and from the engine by means of optical fibres (Figure 1).

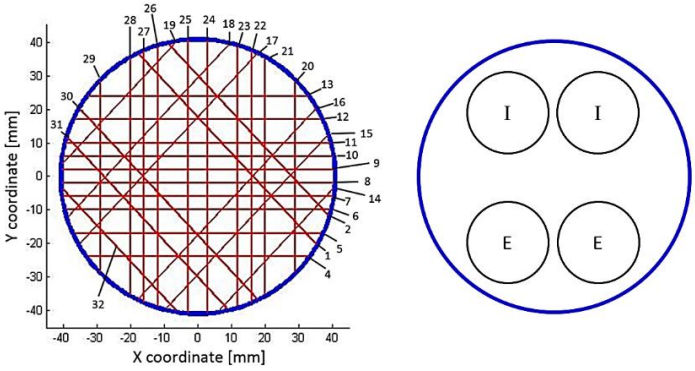


**Figure 1.** Beam array of 31 beams (#1-32, beam #3 was not installed) and location of intake (I) and exhaust (E) valves viewing down into the cylinder towards the crankshaft.

One beam of the array (beam #3) could not be installed for the present work due to its close proximity to the engine's timing belt, therefore 31 beams were installed. On the engine and surrounding the optical access ring, the beams are collimated and launched into the imaging space forming a co-planar grid - the beam array . The imaging space of interest is circular and has a diameter of 81 mm as defined by an optical access ring. The beams traverse the imaging space and the unknown, spatially-varying hydrocarbon distribution *c(x,y)* and is detected using photodiodes.

The imaging technique used for fuel distribution measurement should be minimally-intrusive, chemically selective and faster than the process being imaged. PLIF provides excellent spatial resolution but achieving imaging at a rate of e.g. 10 kHz is difficult given the low pulse energy from high repetition rate lasers. As previously discussed[14,8], the CST system used here meets the requirements for SI engines. CST is readily applicable to multi-cylinder engines and does not require the use of dopants. Consequently, it is ideal for use with multi-component commercial fuel formulations. The spatial resolution of CST has been previously[15] systematically quantified and is, in general, poorer than PLIF as a camera is not used. However, by selecting an adequate number of sampling beams, the spatial resolution can be customised to suit a particular application.

The acquisition speed of the instrument is approximately 100 kHz. However, due to intrinsic properties of the specific photodetectors used here, the acquisition bandwidth of the instrument is reduced to approximately 3 kHz.

In this paper we report the first application of CST using near-IR spectroscopic absorption on an optically accessible CI engine. The installed system was used to visualise the concentration distribution of a hydrocarbon fuel blend under different engine operating conditions. The results from CST were compared with those from PLIF, applied quasi-simultaneously on the same engine and using similar operating conditions.

## Tomography system installation and commissioning

The tomography system was installed on a 2nd generation Volvo D5 engine modified for single cylinder optical operation with Bowditch extension. A circular fused silica optical access ring 2.5 cm high, 81 mm bore formed the top of the combustion chamber. A Bosch injector with seven 0.13 mm holes and a cone angle of 153° was used, fed by an independent fuel rig. The modifications allowed for CST and PLIF optical diagnostics to be performed up to a peak cylinder pressure of 60 bar, a pressure rise rate of 0.8 bar per Crank Angle Degree (CAD) and a maximum body temperature of 80 °C. The piston head was flat-top shaped and made of steel or fused silica for CST and PLIF experiments respectively. A flat-top piston was used to eliminate the lens effect from a bowl type optical piston during PLIF imaging. The engine rotation speed was 1200 RPM. Given the 3 kHz data acquisition bandwidth of the instrument, the temporal resolution was one tomographic frame every 2.4 CAD.

*The fuel*

The fuel used was the same for the PLIF and CST experiments. It consisted of 50% iso-dodecane ('iC12') and 50% n-dodecane ('nC12'), to which 0.03% of PARADYNE-665 was added as a lubricity modifier and 1% naphthalene as a fluorescent tracer for PLIF. The derived cetane number of the blend is 53.9, measured using an Ignition Quality Tester. The contribution of the additives to the spectroscopic absorption signal was assumed to be insignificant.

Long-chain hydrocarbons are susceptible to decomposition by pyrolysis and cracking at elevated pressure and temperature, yielding significantly different spectroscopy. The decomposition of n-dodecane was modelled (Table 1) using a detailed chemical kinetic model composed of 797 species and 4989 reactions using the EXGAS software[16]. Only n-dodecane was modelled as it is more reactive than iso-dodecane. The simulation was performed using the CHEMKIN-PRO software in a closed 1 $cm^3$ reactor and with a nitrogen atmosphere. A simulation for 25 ms represented the compression stroke and one for 50 ms as a worst-case scenario. The converted quantity of n-dodecane remained below 1%. Therefore the experiments and data analysis assume no decomposition of fuel.

**Table 1.** Experimental conditions and results of simulated decomposition of n-dodecane.

| Simulation | $\%X_o$ $C_{12}H_{26}$ | $\%X_o$ $N_2$ | $T$ (K) | $P$ (bar) | $t$ (ms) | %conversion |
|---|---|---|---|---|---|---|
| 1 | 0.05 (5%) | 0.95 (95%) | 875 | 35 | 25 | 0.492 |
| 2 | 0.05 (5%) | 0.95 (95%) | 875 | 35 | 50 | 0.994 |

*The tomography array*

The tomography array forms four angular projections spaced by 45° and consisting of 10-6-10-5 beams. The diameter of the imaging space is 81 mm. A tomographic projection is herein defined as a set of laser beams with the same angular position. The design approach and implementation is similar to the one used in the SI engine study[8], resulting in a quasi-regular grid which closely mimics the array used in an early version of the tomography system[17]. A regular arrangement has been shown[18] to offer uniform and optimum sampling of the Radon space, so efforts were made to achieve this in spite of mechanical obstructions. Light was delivered to, and collected from, the launch/receive optics using optical fibres and collimators mounted on an aluminium plate (hereafter optical mounting plate) in 'V'-shaped grooves[8].

*Installation on the engine*

Both the tomography array and the data acquisition system were installed inside the engine test cell. The optical mounting plate was installed on top of the engine's liner extension plate and accurately located using dowel pins (Figure 2). An optical access ring was manufactured to a concentricity tolerance of 25 µm (Gooch & Housego Ltd., UK) and installed on the liner extension plate using graphite gaskets and made concentric to the bore. Crank-angle encoder and Top-Dead-Centre (TDC) sensor signals were captured for data synchronization.

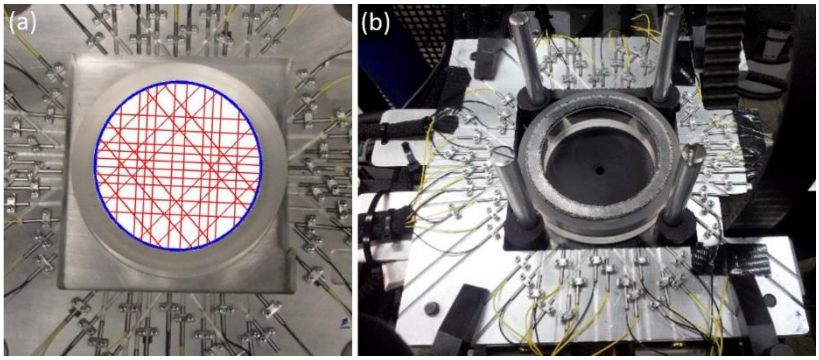


**Figure 2.** Fabricated optical access plate, with the beam array superimposed (a), and the system installed on the engine (b).

The height at which the optical mounting plate (and hence the imaging plane) is positioned above the liner plate is a trade-off between three factors: 1) beam obstruction by the piston, 2) beam obstruction by the intake/exhaust valves and 3) the distance from the injector. The imaging plane was set 6 mm below the bottom of the engine's head. At this level the beams are obstructed for 1 mm of piston travel around TDC which corresponds to an optically inaccessible region of operation of ±18 CAD. This represents an improvement over the ±20 CAD[8] and ±30 CAD[14] previously achieved. Raising the imaging plane by 1 mm would allow for imaging up to and including TDC.

*Optical coupling*

Optical coupling refers to the ratio (≤ 1) of received to launched light intensity between a pair of launch and receive collimators in the absence of absorbing species, here fuel vapour. A higher level of coupling is desirable in order to maintain signal integrity despite beam-steering effects. To check the level and variation of optical coupling, the received light intensity level was recorded for both measurement and reference wavelengths at four stages during experiments.

1) Immediately following installation, all optical surfaces cleaned, coupling optimized;
2) After motoring for 15 minutes;
3) After motoring for a further 30 minutes with intermittent firing (5 s firing out of every 30 s);
4) End of tests, after having cleaned the inside surface of the optical ring.

The intensity levels recorded at stage 1 are treated as a reference as they were captured before engine operation. At stage 2 the received intensity for the majority of beams decreased by typically 10% which we attribute to vibration-induced misalignment of the launch and receive elements and misalignment due to thermal cycling ($\Delta T \approx 40°C$) of the components. At stage 3, 22 out of 31 beams showed further degradation. At stage 4, following cleaning of the internal surface of the optical access ring, 14 out of 31 beams were virtually restored, the rest showing improved coupling. One beam showed an increase in coupling at stage 3 by 200%. We believe this is due to diffraction/scattering effects induced by particle aggregates deposited on the optical ring. This theory is supported by the facts that the coupling is reduced after cleaning (stage 4) and the engine not having been operated between stage 3 and 4.

Overall the optical access method was found to withstand prolonged engine operation without significant or irreversible deterioration of the optical coupling between the launch and receive elements.

*Temporal behavior in motored, non-fueled conditions*

To illustrate features of the data, beams #8, #17, #25, #32 were selected to be representative of the range of angles of incidence to the optical ring, projection and path length of all the beams in the array. During the compression stroke of each engine cycle, the received intensity amplitude of both wavelengths was captured and a boxcar moving-average filter (window size ≈ 0.3 CAD) was applied to suppress high-frequency signals. Subsequently, the ratio of the 1700 nm and the 1651 nm signal amplitudes was taken and normalised to an acquisition taken immediately before non-fueled motoring began i.e. when the engine was static. This process was repeated for 4 engine cycles and the resulting data averaged, yielding the normalised ratiometric data for each beam (Figure 3).

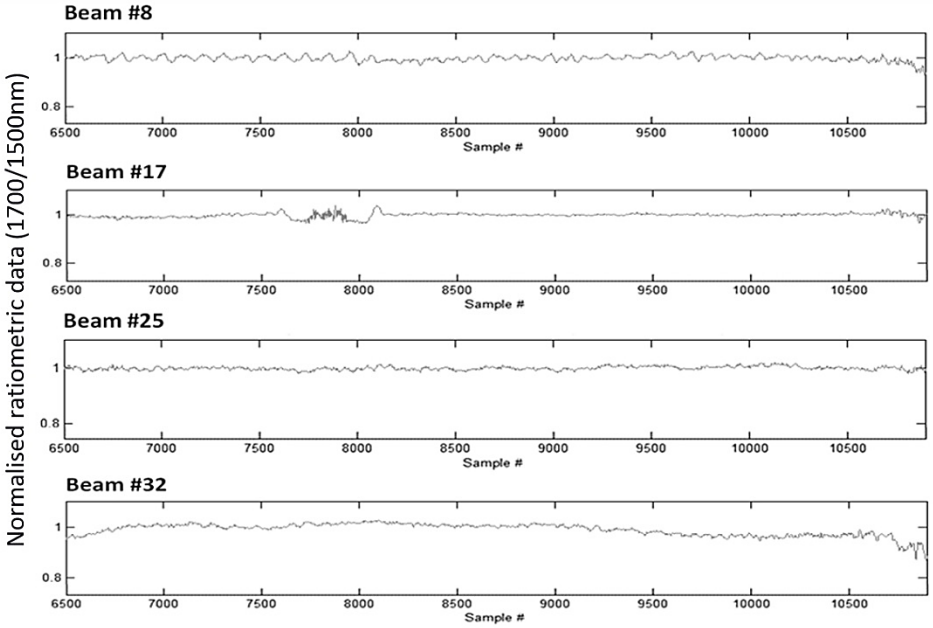


**Figure 3.** Normalised ratiometric data for beams #8, #17, #25 and #32 during the compression stroke in the absence of fuel, averaged over four engine cycles.

Overall the data collected are relatively stable, the deviation from unity being less than 10%. Periodic disturbances can be observed and are more pronounced in beam #8. The fundamental frequency of the disturbances is ≈ 1200 Hz, i.e. 60 times higher than the engine operating speed. The magnitude of the disturbances varies between beams, which suggests that these disturbances are due to vibration-induced etalons. Data from beam #17 indicate a structured feature (between sample 7500 and 8000) with two peaks before and after a high-frequency event, potentially due to a complex vibration interaction between the engine and optical components. In all cases the perturbations described were found to be highly repeatable between engine cycles, allowing for their suppression using referencing techniques.

Following an injection event in a nitrogen atmosphere, traces of fuel remained detectable in the cylinder. Data were monitored at full acquisition rate and compared from cycle to cycle; it was found that they returned to pre-fuelling levels after typically two engine cycles.

## Engine fuel experiments

Data were acquired with the installed tomography system at three different engine operating conditions (step numbers 3, 4 and 5 in Table 2). The intake temperature, injection duration and Start of Injection (SOI) were varied to create qualitatively contrasting mixture strength and evaporation behavior: an earlier SOI and/or a higher intake temperature leading to a more dispersed fuel distribution near TDC. SOI was timed at TDC-100 CAD (steps 3 and 4) and TDC-50 CAD (step 5) in order to study the entire mixing process in more detail. In all cases the engine air intake was substituted with nitrogen gas to prevent combustion. Fuel was injected for single cycles (engine is motored), separated by periods of nine cycles without fuel injection. The first two of the nine cycles were used to, as described previously, purge the cylinder of remaining fuel from the previous injection. The seven remaining cycles were used as a reference for the 10$^{th}$, fueled cycle. The engine fueling and data referencing strategy is described in more detail in the next section and Figure 3.

**Table 2.** Experimental steps and corresponding engine conditions for the fueled engine experiments using CST.

| Step # | Objective | Engine Conditions |
|---|---|---|
| 1 | Full-Scale reference | No obstructions |
| 2 | Control | Motored with air |
| 3 | Fast evaporation<br>Lean mixture<br>Early injection | • Motored+$N_2$+Fuel, SOI @ TDC-100 CAD<br>• Injection duration 0.6 ms, 300 bar<br>• $T_{intake}$ 80 °C |
| 4 (a,b) | Slow evaporation<br>Rich mixture<br>Early injection | • Motored+$N_2$+Fuel, SOI @ TDC-100 CAD<br>• a) Injection duration 0.6 ms, 600 bar<br>b) Injection duration 1.2 ms, 300 bar<br>• $T_{intake}$ 45 °C |
| 5 | Slow evaporation<br>Lean mixture<br>Late injection | • Motored+$N_2$+Fuel, SOI @ TDC-50 CAD<br>• Injection duration 0.6 ms, 300 bar<br>• $T_{intake}$ 45 °C |

*Data conditioning and referencing*

Given the datastream from a single engine cycle (720 CAD), the background minimum received intensities were acquired near the end of the exhaust stroke, from the beginning of the period that the piston obstructs all receivers (TDC-18 CAD) and for a duration of 15 CAD (until TDC-3 CAD). The maximum intensities were acquired during the start of the compression stroke (TDC-180 CAD) and for a duration of 30 CAD (until TDC-150 CAD). The mean of the minimum and maximum intensities were used for offset-correction and scaling respectively. The offset-corrected and scaled intensities at the measurement and reference wavelengths, $I_{\lambda meas}$ and $I_{\lambda ref}$ respectively, were used to compute the in-cycle ratiometric data $T_{in\text{-}cycle}$.

Algorithms that rely on high correlation between two consecutive engine cycles in order to achieve background signal compensation as in the SI engine case[8,14] cannot be applied here due to the variability of the received signals from cycle to cycle in the CI engine case. Instead, the data from seven consecutive non-fueled cycles (*U3-U9*) were averaged and used to reference the following fueled cycle *F* (Figure 4), which can in principle be fired or motored, but is always motored in the work reported here. The collection of 10 engine cycles, nine non-fuelled and one fuelled, is termed a *Sequence*. The first two non-fueled cycles (*U1, U2*) are needed to purge fuel from the previous Sequence.

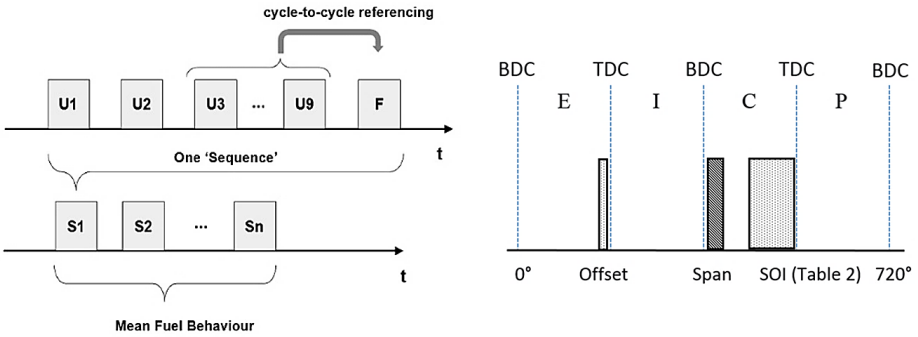


**Figure 4.** Algorithm to process the data from multiple engine cycles (left) and in-cycle data acquisition temporal locations (right).

The image reconstructions from the CI engine data were performed using the mean of two Sequences, corresponding to an effective rate of one tomographic frame every 20 motored cycles. As such, tomographic frames at consecutive CAD timings in the following sections utilise equivalent-time sampling. This was empirically found to produce repeatable results with a cycle-averaged standard deviation less than 10% of the maximum peak-peak transmission signal deviation. As previously stated, the instrument's acquisition rate is one tomographic frame every 2.4 CAD and here we chose to use the frame data with the multi-cycle referencing scheme described above.

*Image reconstruction*

The task of the image reconstruction algorithm is to quantify the hydrocarbon species concentration distribution given a set of path-integral absorption measurements. The number of measurements is substantially lower than the unknowns (image pixels), therefore a direct solution requires prior knowledge about the nature of the concentration distribution[19]. In this work we applied the non-emission

criterion and assumed the distribution to be smooth[20]. The latter assumption, implemented as a spatial filter in the image domain, has been used before in SI engine studies[8,13,14].

A number of algorithms exist for the solution of the inverse problem. An overview[13] and a comparative study[21] have been presented. In this work we chose to use the Landweber iterative reconstruction method as it was developed for systems with a small number of projections (< 100). The parameters of the algorithm, described more fully in[13], were previously[15] optimised for this work by imaging propane distributions in the laboratory. The tomographic reconstructions in this work are qualitative, however quantitative measurements are feasible following studying of the spectroscopic behaviour of the fuel blend in this work. Each set of reconstruction results corresponding to an experimental step (3, 4a, 4b and 5) has been normalised based on the maximum and minimum concentration occuring within that particular set of results.

Prior to image reconstruction, a qualification test was performed on a per-beam basis to prevent spurious input data to the image reconstruction algorithm from impairing the resulting images. The non-emission criterion (below) was applied between SOI and TDC-18 CAD and the remaining criteria between SOI+15 CAD and TDC-18 CAD.

*Non-emission.* Only transmission <1 is plausible. Beams with values 1 - 1.005 were set to 1. Beams with higher values were rejected.

*Smoothness.* The change of transmission $\Delta T_{in\text{-}cycle}$ was calculated over an interval of 5 CAD. The beam in question was rejected if the change was more than 20% of the maximum in-cycle referenced transmission (i.e. if $\text{abs}[T_{in\text{-}cycle}(t) - T_{in\text{-}cycle}(t + 5\ \text{CAD})] > 0.2\ T_{in\text{-}cycle\ max}$), indicating a strong transient effect.

*Severely limited views.* An adequate number of beams must be maintained for meaningful image reconstruction results. If, following application of the non-emission and smoothness criteria, the number of qualifying beams was fewer than 25, the Sequence was rejected and the next Sequence tested.

*Repeatability.* If two consecutive qualifying Sequences were grossly dissimilar, the first one was rejected and the next two compared. This strategy reduced the possibility of fast transient effects impairing the measurements.

## CST results

Examples of the resulting images are shown in Figures 5-8, where the timing of each frame within the compression stroke is relative to TDC. All CST images are qualitative.

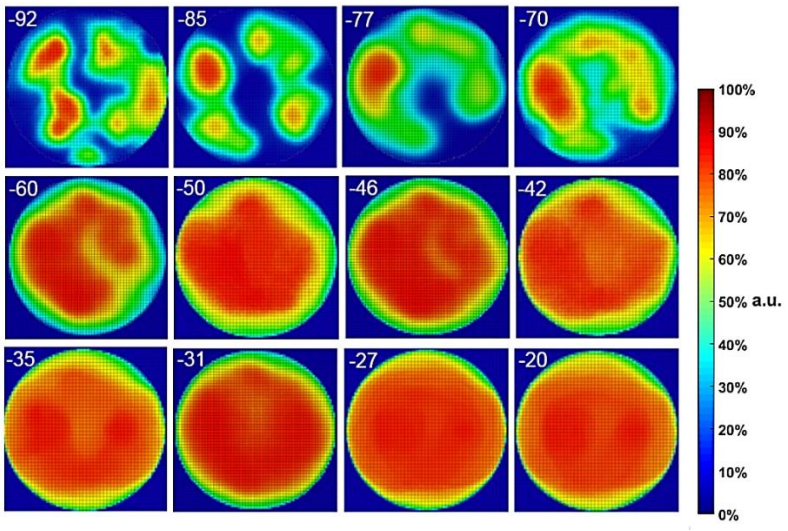


**Figure 5.** Image reconstructions for experimental condition 3. SOI @ TDC-100 CAD, 0.6 ms, 300 bar, 80 °C.

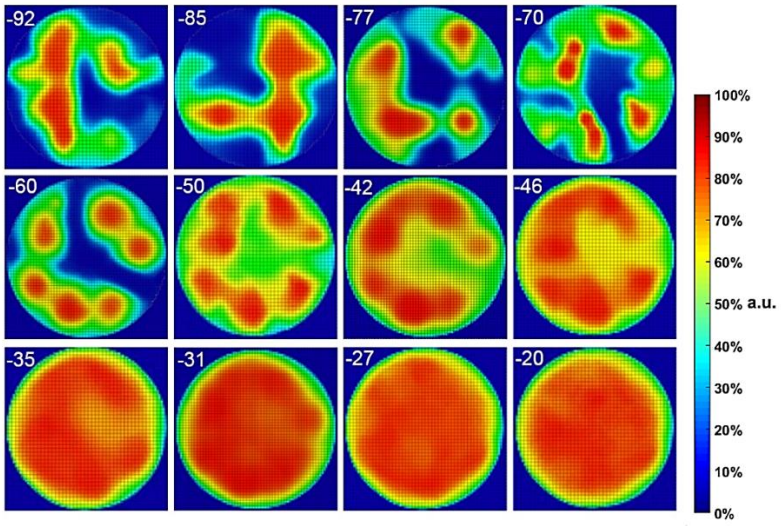


**Figure 6.** Image reconstructions for experimental step 4a. SOI @ TDC-100 CAD, 0.6 ms, 600 bar, 45 °C.

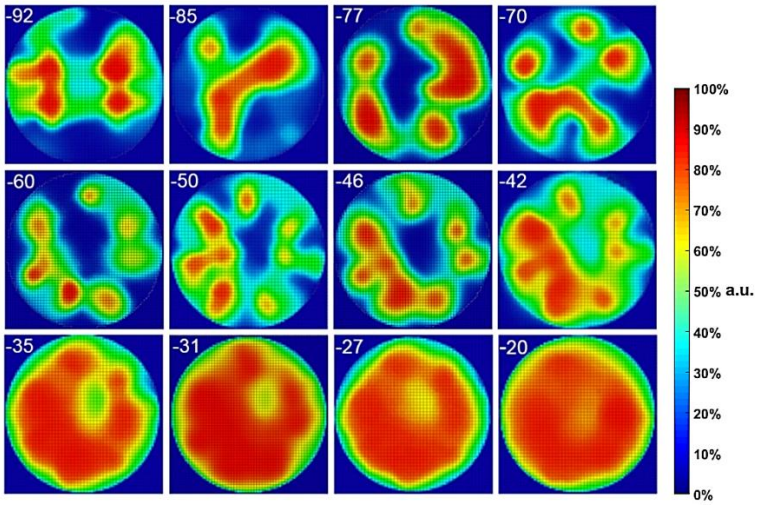


**Figure 7.** Image reconstructions for experimental step 4b. SOI @ TDC-100 CAD, 1.2 ms, 300 bar, 45 °C.

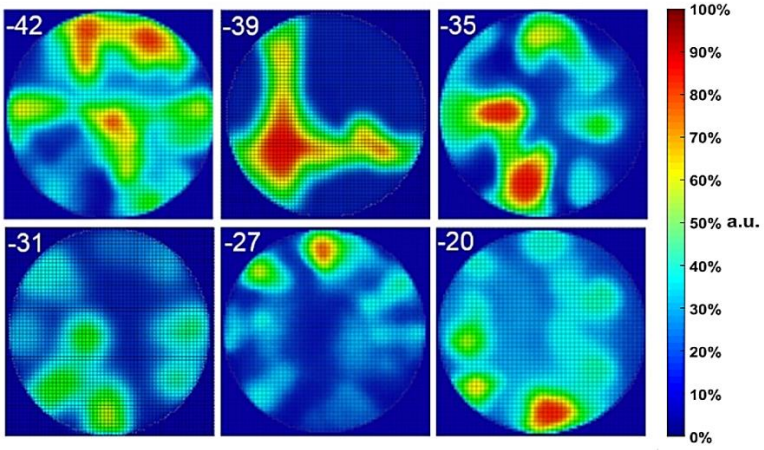


**Figure 8.** Image reconstructions for experimental step 5. SOI @ TDC-50 CAD, 0.6 ms, 300 bar, 45 °C.

The timings of the reconstructed images presented in Figures 5 to 8 were selected to uniformly sample the duration between SOI and TDC-20 CAD. In between the timings presented, the reconstructed images did not demonstrate substantial variability. Examining the reconstructions of Figures 5 to 8, it can be observed that the images very soon after injection, e.g. at SOI+8 CAD, do not correlate with the expected injection pattern from a seven-hole injector, which is seven clearly distinct fuel-rich regions in the imaging space. Strong localised artefacts are generated that vary substantially between

experimental conditions. Related behaviour has been observed in previous SI engine works[8,14] where the discrimination of droplets within the fuel spray was reconstructed purely from attenuation of the reference wavelength. Immediately following injection, the fuel is largely in the liquid phase and the refraction effects from fuel droplets are severe for both wavelengths. Unequal refraction between the absorbed and reference wavelengths (dispersion) can introduce a false differential signal and ultimate degradation of the SNR.

As evaporation of the injected fuel subsequently takes place, the fuel droplets reduce in size and count. The aggregate effect is the integrity of the DWR method being steadily restored, as observed in Figures 5 and 8 at SOI+15 CAD where the reconstructed features are in closer agreement with the expected fuel distribution at those stages in the engine cycle. However, in Figures 6 and 7 at the same temporal position (SOI+15 CAD), the reconstructions suggest that a significant proportion of fuel remains in the liquid phase, a systematic behavior that was observed in four Sequences. The delayed evaporation can be attributed to the lower intake temperature (45 °C as opposed to 80 °C) and the greater (approximately double) amount of fuel injected.

As evaporation progresses from SOI+30 CAD onwards, the first fuel-rich pockets are successfully reconstructed for all experimental conditions. Over time the fuel rich pockets disperse, forming an annular high-concentration region near the walls of the imaging space (i.e. the cylinder). The amount of fuel in the centre of the cylinder remains comparatively smaller than that in the outer ring as mixing occurs, which can be attributed to the injector geometry (153° injection angle). Nearing TDC, fuel occupies the majority of the imaging space and the mixture approaches homogeneity: in Figure 5, where evaporation is promoted by a higher intake temperature, homogenisation is apparent as early as TDC-50 CAD; in contrast, in Figure 7 where evaporation is suppressed by a lower intake temperature and longer injection duration, homogenisation is approached 23 CAD later, at TDC-27 CAD. The average concentration in Figure 8 is notably more localised than in the other conditions. We attribute this to the combination of a shorter injection duration and lower intake temperature that combine to delay dispersion of the fuel mixture (compared with Figures 7 and 5 respectively). Moreover, at the time of injection in Figure 8 (compression stroke TDC-50 CAD) the pressure inside the combustion chamber is higher than in the other conditions, resulting in lowering of the spectroscopic absorption signal due to broadening effects[17] and therefore reduced sensitivity to low fuel concentrations.

## PLIF imaging

The quasi-simultaneous CST and PLIF imaging capability was utilised by capturing PLIF images at a subset of the CST experimental conditions (Table 3) and using the same fuel blend. The PLIF image processing algorithm uses the 'flat-field' correction technique[22]. For each processed image a total of 100 raw images were captured of a) a near-homogeneous mixture, b) the background (no fuel) and c) at the desired timing. The PLIF laser repetition rate was 10 Hz and equivalent-time sampling was employed. All of these conditions are typical of PLIF implementations in engine research[12]. The PLIF conditions 3(a-d) are equivalent to the CST condition 4(b), and the PLIF conditions 6(a-d) are equivalent to CST condition 5. The orientation of the PLIF images is identical to the tomographic reconstructions; the intake valves at the bottom and the laser sheet entering from the top of the image.

**Table 3.** PLIF experimental conditions.

| Step # | Objective | Engine Conditions | Capture timing |
|---|---|---|---|
| 1 | Acq. background | Motored with air | TDC-20 CAD |
| 2 | Acq. full scale ref | • Motored+$N_2$+Fuel<br>• 1.2 ms, 300 bar, SOI @ TDC-150 CAD<br>• $T_{intake}$ 80 °C | TDC-20 CAD |
| 3 (a-d) | Rich mixture<br>Fast evaporation | • Motored+$N_2$+Fuel<br>• 1.2 ms, 300 bar, SOI @ TDC-100 CAD<br>• skipfuel 1 cycle in 10<br>• $T_{intake}$ 80 °C | a) TDC-92 CAD<br>b) TDC-85 CAD<br>c) TDC-50 CAD<br>d) TDC-20 CAD |
| 4 | Acq. background | • Motored with air | TDC-20 CAD |
| 5 | Acq. full scale ref | • Motored+$N_2$+Fuel<br>• 0.6 ms, 300 bar, SOI @ TDC-150 CAD<br>• $T_{intake}$ 45 °C | TDC-20 CAD |
| 6 (a-d) | Lean mixture<br>Slow evaporation | • Motored+$N_2$+Fuel<br>• 0.6 ms, 300 bar, SOI @ TDC-50 CAD<br>• skipfuel 1 cycle in 10<br>• $T_{intake}$ 45 °C | a) TDC-42 CAD<br>b) TDC-35 CAD<br>c) TDC-27 CAD<br>d) TDC-20 CAD |

## PLIF results

The resulting processed images (Figure 9) from each experimental condition are presented in monochrome, iso-intensity and 'jet' colour palette, the last of these being identical to the presentation of the tomographic reconstructions. All PLIF images are qualitative.

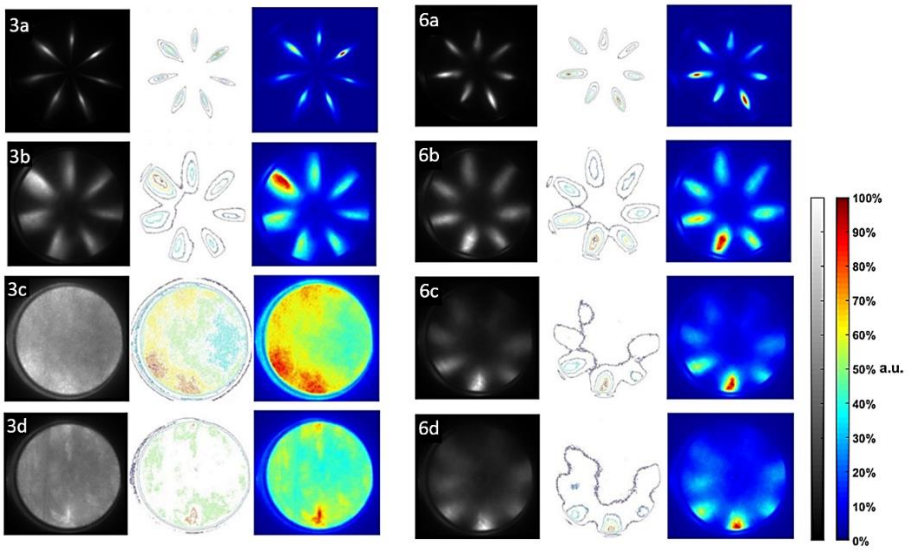


**Figure 9.** Results from PLIF imaging at experimental conditions according to Table 3. For both experimental conditions, the leftmost columns are the processed images without false colouring. The middle columns indicate contours of equal intensity (iso-intensity plot). The rightmost columns have been coloured using the Matlab 'jet' palette to match the CST images. The acquisition timing following SOI increases from top to bottom as per Table 3.

At SOI+8 CAD (condition 3a), the injection pattern is clearly visible, with increased dispersion at SOI+15 CAD (condition 3b) and mixing at SOI+50 CAD (condition 3c). Finally, homogeneity is approached at SOI+80 CAD (condition 3d) as seen in the iso-intensity image. Condition 6a demonstrates similar characteristics to 3a. At conditions 6b to 6d the mixture becomes increasingly dispersed, but not to the same extent as in the longer period 3b to 3d. Comparing the location of the fuel-rich region near the bottom of conditions 6b to 6d, a counter-clockwise rotating motion of the fuel jets can be observed. This phenomenon, also known as swirl, is also seen at condition 3b, where a counter-clockwise preferential dispersion of the fuel can be observed. The observation of a bulk swirl motion of partially mixed fuel is to be expected from the Volvo D5 engine which supports swirl as a way of generating turbulence in order to improve fuel-air mixing[23]. The swirl motion has been optically recorded in the past using a similar type (direct-injection HCCI), heavy-duty engine[24].

## Co-validation of PLIF and CST

The CST and PLIF images were compared. In this study, the PLIF images are treated as the reference and assumed to be qualitatively representative of the physical fuel distribution beyond the spatial resolution limit of the CST system. To the authors' best knowledge this is the first time such a comparison has been made. Feature localisation and tracking, as well as imaging of a homogeneous distribution, are compared in the discussion below. Due to the strict qualification tests applied to CST data from individual beams (see §*Image Reconstruction*) it was not possible to generate images at precisely identical CAD timings for PLIF and CST. This however did not prevent comparison of CST and PLIF images of adequately small temporal separation in order to reach conclusions regarding the aforementioned feature localisation, tracking and homogeneous mixture imaging. Images in Figures 10 and 11 have been normalised against the maximum and minimum values occurring within each image. Images in Figure 11 were normalised against the maximum and minimum values occurring across all images in a row.

### *Feature localisation*

High-concentration regions in Figure 10 were marked with circles, their centres projected to the centre of the imaging space. In the stratified PLIF case (Figure 10a) the angular separation $\theta$ of the centres is approximately 50°. In the corresponding tomographic reconstruction (Figure 10b) the maximum angular separation varies between 60° and 40°, i.e. ± 10° compared to PLIF. However, as the fuel mixes and disperses over time (Figure 10d and 10c), the centres of the high-concentration regions move within

the imaging space quasi-stochastically. As a result the angular separation between centres varies significantly in both PLIF and tomographic images.

An additional discrete high-concentration region can be seen in the tomographic reconstruction of Figure 10b, marked 'Region B', resulting in a total of eight discrete high-concentration regions. Given that the injector has only seven orifices, this phenomenon can be attributed to injector fouling/deposits or an image reconstruction artefact. Although the engine was not fired in this work, other fuel experiments utilized the test-bed over the same period. The phenomenon was repeatedly observed in the tomographic reconstructions over a number of consecutive engine cycles (*Repeatability* qualification test, see §*Image Reconstruction*). None of the scenarios can be ruled out based on the corresponding PLIF results as the tomography experiments were not performed fully concurrently. We briefly comment on each scenario.

Firstly, injector fouling is known to degrade the injector spray pattern geometry leading to increased spray asymmetry[25]. Here, fuel from one orifice could be breaking up into two discrete jets both of which are captured and reconstructed. Secondly, image reconstruction artefacts can appear in limited-views tomography either as a consequence of the reconstruction algorithm or due to the beam array geometry having a high density of sampling beams in the area that the artifact appears. The high density of sampling beams increases the local sensitivity of the tomograph, thereby a higher fuel concentration is reported than actually present. In turn this gives the impression that a discrete pocket of fuel is present. Region B was treated as an artefact and excluded from the feature localization analysis.

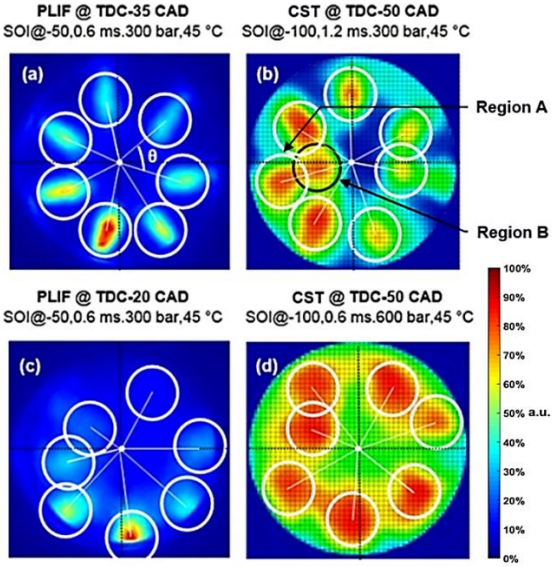


**Figure 10.** (a), (c) PLIF captures and (b), (d) CST reconstructions at similar experimental conditions.

### *Imaging of a homogeneous distribution*

The PLIF and CST images of a quasi-homogeneous distribution are now compared. In the PLIF capture in Figure 11, fine structures are distinguishable in the imaging space. In the CST reconstruction such structures are not observable. In region D of the CST reconstruction the fuel concentration appears to be lower. This is potentially an artefact resulting from a single beam removed for mechanical clearance. Also in the same image, a lower concentration 'ring' on the circumference of the imaging space can be observed (yellow), attributed to the lack of beams near the edges of the imaging space. Two regions of apparently lower concentration (regions C) are observed at the top and bottom of the reconstruction.

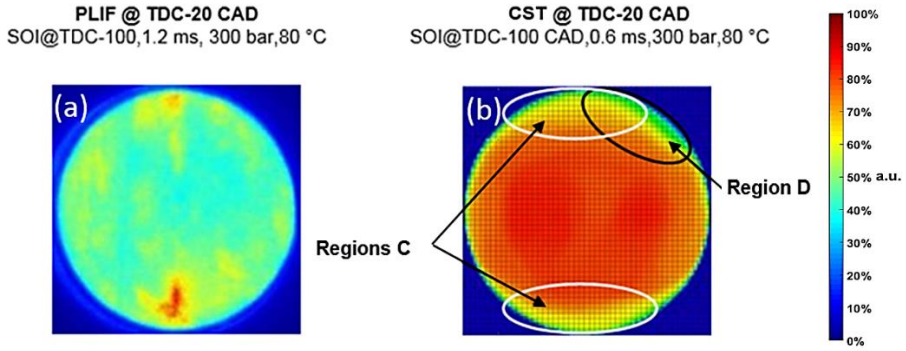


**Figure 11.** PLIF (a) and CST (b) results for a quasi-homogeneous distribution.

*Observed swirl*

As noted above, a swirling motion of the fuel-rich pockets can be observed in the PLIF images. In Figure 12, a fuel-rich pocket is marked in a selection of PLIF and CST images and its centre of maximum intensity projected to the origin of the imaging space. The angle formed to the y axis is tracked as a function of CAD timing. The first image is used as the reference.

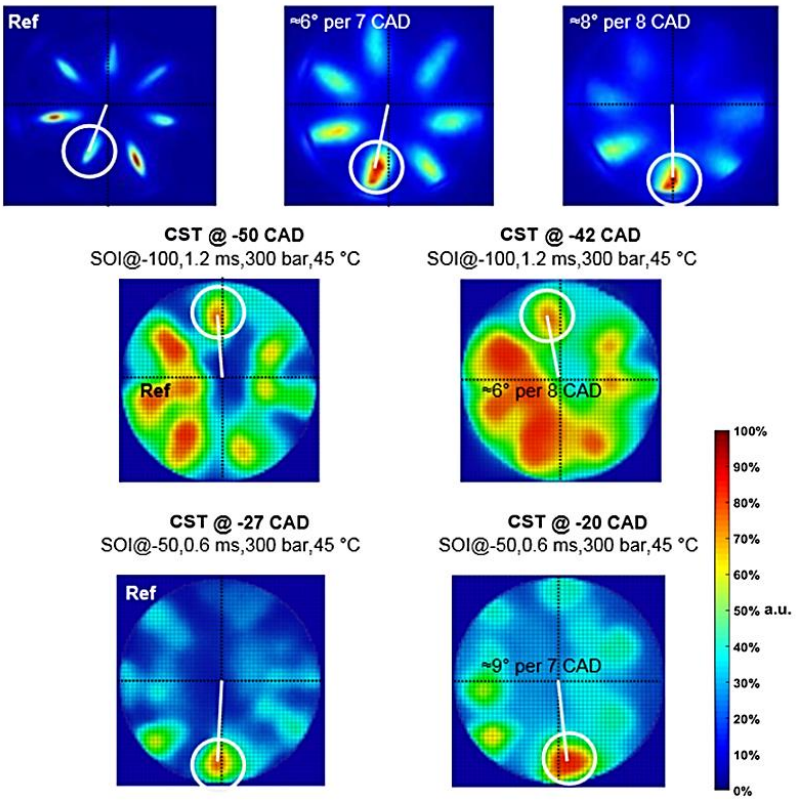


**Figure 12.** High-concentration feature tracked over time in PLIF and CST images.

From the PLIF images it can be deduced that the marked feature rotates by approximately 1° per CAD. The same behaviour is observed for the features marked in the CST images, suggesting that the air/nitrogen mixture rotates counter-clockwise (viewed from top of engine) inside the combustion chamber as it mixes. Most importantly, the cross-validation of this behaviour suggests that the features reconstructed using CST are not artefacts, even though they are reporting only two cycles as opposed to the 100 cycles used in the PLIF sequence. Moreover, CST provides temporal resolution of 1 CAD or better, on a continuous basis, in contrast to the PLIF method.

## Summary & Conclusions

In this paper we have provided a detailed account of the key steps undertaken in applying Chemical Species Tomography by spectroscopic absorption in an optically-accessible CI engine. The objectives and opto-mechanical challenges faced when designing a robust optical access scheme and laser beam array have been described for a 31-beam array. The resilience of a rigidly-mounted optical access plate to the engine is verified by in-situ commissioning tests. Using the implemented system we have demonstrated qualitative imaging of the in-cylinder concentration distribution of an iso/n-dodecane fuel blend in a nitrogen atmosphere, visualising the mixing process under a variety of operating conditions. The results suggest that the intake temperature has a predominant role in determining the speed at which the mixture approaches homogeneity. We demonstrated the first cross-comparison of tomography results with PLIF in terms of feature localization, flat-field imaging and tracking of features in the imaging space. The comparison results encourage further work towards a hybrid diagnostic system of improved spatio-temporal resolution.


### Acknowledgements

This work was supported by the Engineering and Physical Sciences Research Council (EPSRC) under an Engineering Doctorate Programme at The University of Manchester and Shell Global Solutions UK.

**References**


1. Herner JD, Hu S, Robertson WH, Huai T, Chang M-CO, Rieger P, et al. Effect of Advanced Aftertreatment for PM and NOx Reduction on Heavy-Duty Diesel Engine Ultrafine Particle Emissions. Environ Sci Technol. 2011 Mar 15;45(6):2413–9.

2. Schumann B, Alkemade UG. Engines and exhaust after treatment systems for future automotive applications. Solid State Ion. Solid State Ion. 2006;177(26):2291–6.

3. Bradley D, Kalghatgi GT. Influence of autoignition delay time characteristics of different fuels on pressure waves and knock in reciprocating engines. Combust Flame. 2009 Dec;156(12):2307–18.

4. Kalghatgi GT, Hildingsson L, Harrison AJ, Johansson B. Autoignition quality of gasoline fuels in partially premixed combustion in diesel engines. Proc Combust Inst. 2011;33(2):3015–21.

5. Kalghatgi GT, Risberg P, Angstrom H-E. Partially Pre-Mixed Auto-Ignition of Gasoline to Attain Low Smoke and Low NOx at High Load in a Compression Ignition Engine and Comparison with a Diesel Fuel [Internet]. Warrendale, PA: SAE Technical Paper; 2007 Jan [cited 2015 Oct 18]. Report No.: 2007-01–0006. Available from: http://papers.sae.org/2007-01-0006/

6. Kalghatgi GT, Risberg P, Ångström H-E. Advantages of Fuels with High Resistance to Auto-ignition in Late-injection, Low-temperature, Compression Ignition Combustion [Internet]. Warrendale, PA: SAE Technical Paper; 2006 Oct [cited 2015 Oct 18]. Report No.: 2006-01–3385. Available from: http://papers.sae.org/2006-01-3385/

7. Sick V. High speed imaging in fundamental and applied combustion research. Proc Combust Inst. 2013;34(2):3509–30.

8. Terzija N, Karagiannopoulos S, Begg S, Wright P, Ozanyan K, McCann H. Tomographic imaging of the liquid and vapour fuel distributions in a single-cylinder direct-injection gasoline engine. Int J Engine Res. 2015 Jun 1;16(4):565–79.

9. Dyer MJ, Crosley DR. Two-dimensional imaging of OH laser-induced fluorescence in a flame. Opt Lett. 1982 Aug 1;7(8):382.

10. Beeck M-A, Hentschel W. Laser metrology — a diagnostic tool in automotive development processes. Opt Lasers Eng. 2000 Aug;34(2):101–20.

11. Hanson RK, Seitzman JM, Paul PH. Planar laser-fluorescence imaging of combustion gases. Appl Phys B. 1990 Jun;50(6):441–54.

12. Schulz C, Sick V. Tracer-LIF diagnostics: quantitative measurement of fuel concentration, temperature and fuel/air ratio in practical combustion systems. Prog Energy Combust Sci. 2005;31(1):75–121.

13. Terzija N, Davidson JL, Garcia-Stewart CA, Wright P, Ozanyan KB, Pegrum S, et al. Image optimization for chemical species tomography with an irregular and sparse beam array. Meas Sci Technol. 2008;19(9):94007.

14. Wright P, Terzija N, Davidson JL, Garcia-Castillo S, Garcia-Stewart C, Pegrum S, et al. High-speed chemical species tomography in a multi-cylinder automotive engine. Chem Eng J. 2010 Mar 15;158(1):2–10.

15. Tsekenis SA, Tait N, McCann H. Spatially resolved and observer-free experimental quantification of spatial resolution in tomographic images. Rev Sci Instrum. 2015 Mar 1;86(3):35104.

16. Biet J, Hakka MH, Warth V, Glaude P-A, Battin-Leclerc F. Experimental and modeling study of the low-temperature oxidation of large alkanes. Energy Fuels. 2008 Jul;22(4):2258–69.

17. Hindle FP, Carey SJ, Ozanyan K, Winterbone DE, Clough E, McCann H. Measurement of gaseous hydrocarbon distribution by a near-infrared absorption tomography system. J Electron Imaging. 2001;10(3):593–600.

18. Rattey P, Lindgren AG. Sampling the 2-D Radon transform. IEEE Trans Acoust Speech Signal Process. 1981 Oct;29(5):994–1002.

19. Herman GT. Fundamentals of Computerized Tomography: Image Reconstruction from Projections. Springer Science & Business Media; 2009. 302 p.

20. Feng J, Bao S l. Reconstruction of smooth distributions within unsmooth circumferences from limited views using filtered-backprojection algorithm. Int J Imaging Syst Technol. 2002 Jan 1;12(3):93–6.

21. Verhoeven D. Limited-data computed tomography algorithms for the physical sciences. Appl Opt. 1993 Jul 10;32(20):3736–54.

22. Seibert JA, Boone JM, Lindfors KK. Flat-field correction technique for digital detectors. In San Diego, CA: SPIE; 1998 [cited 2015 Oct 19]. p. 348–54. Available from: http://dx.doi.org/10.1117/12.317034

23. Miles PC, Collin R, Hildingsson L, Hultqvist A, Andersson Ö. Combined measurements of flow structure, partially oxidized fuel, and soot in a high-speed, direct-injection diesel engine. Proc Combust Inst. 2007 Jan;31(2):2963–70.

24. Särner G, Richter M, Aldén M, Hildingsson L, Hultqvist A, Johansson B. Simultaneous PLIF Measurements for Visualization of Formaldehyde- and Fuel- Distributions in a DI HCCI Engine. In 2005 [cited 2016 Nov 6]. Available from: http://papers.sae.org/2005-01-3869/

25. Barker J, Richard P, Snape C, Meredith W. Diesel Injector Deposits - An Issue That Has Evolved with Engine Technology. In 2011 [cited 2016 Nov 6]. Available from: http://papers.sae.org/2011-01-1923/